



Topology Optimization for Design of Hybrid Lattice Structures with Multiple Functional Microstructure Configurations

Yifan Guo¹ , Yongsheng Ma²  and Rafiq Ahmad³ 

¹University of Alberta, guo15@ualberta.ca

²Southern University of Science and Technology, mays@sustech.edu.cn

³University of Alberta, Rafiq.Ahmad@ualberta.ca

Corresponding author: Yongsheng Ma, mays@sustech.edu.cn
Rafiq Ahmad, Rafiq.Ahmad@ualberta.ca

Abstract. The paper proposes a method based on topology optimization and homogenization theory to design hybrid lattice structures with multiple functional microstructure configurations. A hybrid lattice structure with low thermal expansion and higher stiffness is designed to validate the feasibility of this method. The numerical experimental results show that the maximum thermal distortion of the optimized lattice structure is only 10% of that of the macroscopic solid-void structures. Meanwhile, the optimized lattice structure achieves an 18% reduction in compliance compared with the macroscopic solid-void structure.

Keywords: Topology optimization, Hybrid lattice structures, thermal expansion.

DOI: <https://doi.org/10.14733/cadaps.2023.946-959>

1 INTRODUCTION

Lattice structures (LSs) have been an emerging solution for lightweight and mechanically efficient structures [3, 6, 15]. A lattice structure is formed by a regular arrangement of unit cells within a special pattern. The properties of LSs not only depend on the inherent material composition but the architecture of the microstructure. Based on this principle, researchers have designed various LSs with some excellent properties, such as negative Poisson's ratio [11,22], extreme thermal expansion [4, 12], and energy absorption [1, 5]. These lattice structures hold the promise of pursuing excellent multi-functional performances compared with the conventional macroscopic solid-void structures.

The design of the lattice structure mainly depends on the homogenization method. In this method, the homogenous materials are employed as a basis for defining the shape of the object in terms of material density [2]. To obtain better properties of LSs, topology optimization is usually applied with the homogenization method. Topology optimization works on a specific finite element mesh of discrete or continuum elements to optimally sort materials in material layout [13]. By pairing these two, multiscale topology optimization for LSs is rapidly becoming a research hotspot [7, 9, 10,

19, 21]. In addition, many methodologies for hybrid lattice structures (HLSs) design have been proposed since HLSs usually have higher performance and greater design freedom than lattice structures with a single unit cell; for instance, Benjamin developed a framework for the parametric design of graded truss lattice structures for enhanced thermal dissipation [16]. Through the above literature review, it could be found that the existing LSs design methods still could have two points to improve. The one is for the most design method, the microstructures are used standard unit cells, like BCC, FCC unit cells. These unit cells limit the design freedom since they can only change their size instead of their topology. Another is that most microstructure layout methods refer to topology optimization with solid material. However, the layout should be changed if various functional microstructures are applied. The existing layout methods are not suitable for multiple functional unit cells anymore.

To improve LSs structure in the above two points. A novel method based on topology optimization and homogenization theory is given here. Topology optimization is applied for designing various functional microstructures instead of standard unit cells. Then for the layout of various functional microstructures. Topology optimization is applied again, and the ordered SIMP (Solid isotropic material with penalization) method [23, 24] replaces the ordinary SIMP Method for various microstructures interpolation. The flow chart of the proposed method is shown in Figure 1. There are two steps in this method. At first, multiple functional microstructure lattice units are designed through topology optimization and homogenization theory. Then, the lattice units are treated as homogeneous materials with effectively homogenized properties for macroscopic analysis. The ordered SIMP (Solid isotropic material with penalization) interpolation method is applied to achieve the interpolation of multiple microstructures. Finally, the obtained hybrid lattice structure theoretically has both the properties of macroscopic optimization and the functionalities of microstructures. Both the microstructure and macrostructure design variables are updated by the Method of Moving Asymptotes (MMA) algorithm [14].

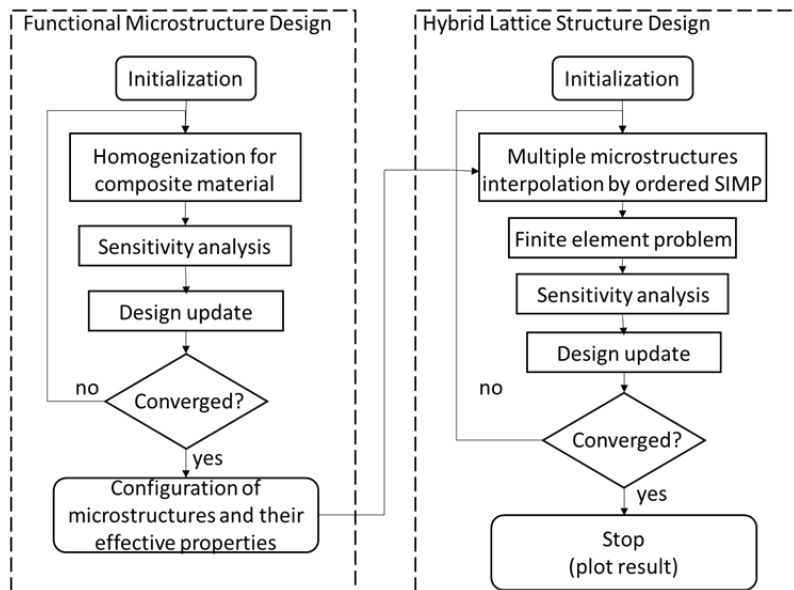


Figure 1: Flow chart of the proposed method.

In this work, the functional microstructure is set to be zero thermal expansion coefficient, and a standard minimized compliance problem is considered on a macroscale. The structure with both low

thermal expansion and high stiffness can be used in many fields, such as aero-engine blades, transmission lines, and bimetallic strips. Numerical examples and data comparisons are presented to demonstrate the validity of the proposed method.

2 FUNCTIONAL MICROSTRUCTURE DESIGN WITH ZERO THERMAL EXPANSION

In this section, a numerical procedure for 2D thermal elastic microstructure topology optimization of three-phase materials (two solid and one void materials, the properties are shown in Table 1.) is introduced, whose optimization model can be expressed as:

$$\left\{ \begin{array}{l} \min: f(x,y) = (\alpha_{11}^H(x,y))^2 + (\alpha_{22}^H(x,y))^2 \\ \text{subject to: } \left\{ \begin{array}{l} V_1 = \frac{1}{V} \sum_{e=1}^{NE} x_e(1-y_e)v_e; V_1^{Low} \leq V_1 \leq V_1^{Up} \\ V_2 = \frac{1}{V} \sum_{e=1}^{NE} x_e y_e v_e; V_2^{Low} \leq V_2 \leq V_2^{Up} \\ K \geq K_{set} \end{array} \right. \end{array} \right. \quad (2.1)$$

	Young's moduli E^i	Passion ratio ν	Thermal expansion coefficient α^i
Solid material 1	145MPa	0.3	0.5×10^{-4}
Solid material 2	290MPa	0.3	2.2×10^{-4}

Table 1: The mechanical properties of solid material.

where α_{ii}^H ($i = 1$ or 2) is the effective thermal expansion tensor that indicates the thermal strain of the composite material in two normal directions under unitary temperature change. The H in the upper right corner of the tensor refers to the fact that this tensor comes from the homogenization method. V_1 and V_2 are two volume fractions for two solid materials. V is the volume of the whole domain. v_e is the volume of the element. NE is the number of elements. x and y are two design variables for those two solid materials. To avoid singularity, the "void" phase is taken as a small number 10^{-4} times material tensors of phase solid material 1. V_i^{Low} and V_i^{Up} ($i = 1$ or 2) is the predefined upper and lower volume fraction limits of two solid materials, and the difference between the upper and lower limits is less than 0.1 so that the value of the volume fraction can be controlled. Generally, zero thermal expansion design is usually achieved at the expense of the overall stiffness of the composite. Thus, a lower bound constraint on the overall composite stiffness ($K \geq K_{set}$) is introduced here to ensure the composite stiffness performance. K indicates the effective bulk moduli, which can be expressed in terms of the components of the effective elasticity tensor C^H :

$$K = 0.25C_{11}^H + 0.25C_{12}^H + 0.25C_{21}^H + 0.25C_{22}^H \quad (2.2)$$

and K_{set} is the prescribed minimum bulk moduli value.

The effective properties of the microstructure can be obtained by using homogenization theory; the effective elasticity tensor C_{pqrs}^H and thermal strain tensor β_{pq}^H can be written as:

$$C_{pqrs}^H = \frac{1}{|Y|} \int_Y C_{pqrs}^e (\epsilon_{pq}^0 - \epsilon_{pq}) (\epsilon_{rs}^{0(ij)} - \epsilon_{rs}^{ij}) dy \quad (2.3)$$

$$\beta_{pq}^H = \frac{1}{|V|} \int C_{pqrs}^e (\alpha_{pq}^e - \epsilon_{pq}) (\epsilon_{rs}^{0(ij)} - \epsilon_{rs}^{ij}) dV \quad p, q, r, s = 1, 2. \quad (2.4)$$

where $|Y|$ denotes the volume of the unit cell and ϵ^0 is known as a test strain field. ϵ is the virtually local strain field, which are defined as:

$$\varepsilon_{pq} = \varepsilon_{pq}(\chi) = \frac{1}{2}(\chi_{p,q} + \chi_{q,p}) \tag{2.5}$$

based on the displacement fields χ found by solving the elasticity equations with a prescribed macroscopic strain,

$$\int_V \mathbf{C}_{ijpq}^e \varepsilon_{ij}(\mathbf{v}) \varepsilon_{pq}(\chi) dV = \int_V \mathbf{C}_{ijpq}^e \varepsilon_{ij}(\mathbf{v}) \varepsilon_{pq}^0 dV \tag{2.6}$$

where \mathbf{v} is a virtual displacement field. The homogenization is performed numerically by discretizing and solving Eq. (2.6) using the finite element method. The detailed homogenization procedure can be found in [20], \mathbf{C}_{ijpq}^e and α_{pq}^e are the locally varying stiffness tensor and local thermal strain tensor, respectively. The e in the upper right corner of the tensor refers to the fact that this tensor is associated with elements. They can be interpolated by the extended SIMP interpolation scheme; it can be formulated as:

$$\mathbf{C}_{ijpq}^e(x_e, y_e) = x_e^P \cdot (y_e^P \cdot \mathbf{C}_{ijpq}^2 + (1 - y_e)^P \cdot \mathbf{C}_{ijpq}^1) \tag{2.7}$$

$$\alpha_{ij}^e = y_e^P \cdot \alpha_{ij}^2 + (1 - y_e)^P \cdot \alpha_{ij}^1 \tag{2.8}$$

where \mathbf{C}_{ijpq}^j and α_{ij}^j ($j = 1$ or 2) represent the stiffness tensor and thermal strain coefficient tensor for solid material 1 and solid material 2, respectively. The equivalent thermal expansion tensor α_{ij}^H can be calculated by:

$$\alpha_{ij}^H = (\mathbf{C}_{pqrs}^H)^{-1} \beta_{pq}^H \tag{2.9}$$

In this paper, the design domain is set to be **20mm × 20mm** size square. For the isotropic design, symmetry is assumed along the center and diagonal lines of the square design domain. There is also a forced removal of the material domain, in which no material can exist, to maintain sufficient space for thermal deformation. And the composite joint domain is set to be solid, which also can be regarded as a deformation evaluation domain. The design domain is discretized by 200×200 four-node quadrilateral elements. The whole domain and its distribution are shown in Figure 2.

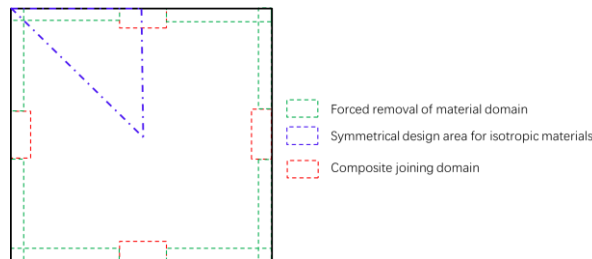



Figure 2: Design domain for functional microstructure, the width of the green domain is 1mm, and the size of the red domain is 2mm × 1mm .

Finally, after setting three different volume fractions for different materials, and the temperature difference is determined to be 30 degrees, three designed zero thermal expansion microstructures are obtained and shown below table:

	V_x	V_y	Configuration	Bulk moduli K	Objective function f	Effective elastic tensor C_{pqrs}^H
Microstructure1	0.2	0.2		100	$0.8787E - 5$	$\begin{bmatrix} 112.55 & 87.44 & 0 \\ 87.44 & 112.55 & 0 \\ 0 & 0 & 48.88 \end{bmatrix}$


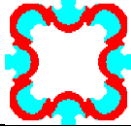
Microstructure2	0.25	0.25		150	$0.1395E - 5$	$\begin{bmatrix} 186.44 & 113.56 & 0 \\ 113.56 & 186.44 & 0 \\ 0 & 0 & 85.25 \end{bmatrix}$
Microstructure3	0.3	0.3		200	$0.2747E - 5$	$\begin{bmatrix} 261.85 & 138.44 & 0 \\ 138.44 & 261.85 & 0 \\ 0 & 0 & 48.88 \end{bmatrix}$

Table 2: The mechanical properties of three pre-designed microstructures.

The heat deformations for three microstructures in Table 2 are shown below. Since the microstructures shown in Table 2 are symmetric, it can apply symmetric boundaries on the left and bottom edges of Figure 3 and 4 to save the computational cost. Figure 3 only shows the deformation on the joint to highlight the deformation on the joint; Figure 4 demonstrates the deformation of the whole domain. The maximum displacement on the joint for microstructure1 is 3.67×10^{-3} mm, for microstructure2 is 4.33×10^{-3} mm, and 8.14×10^{-3} mm for microstructure3. As Figure 4 shows, the maximum displacement for the whole structure is 4.72×10^{-2} mm, 4.43×10^{-2} mm, and 4.66×10^{-2} mm for microstructure1, microstructure2, and microstructure3, respectively. These results show that thermal expansion is not proportional to volume fraction. Therefore, it's hard to say which microstructure has the best thermal properties. The hybrid lattice structure will be necessary to enlarge the design space and does not converge into a single microstructure.

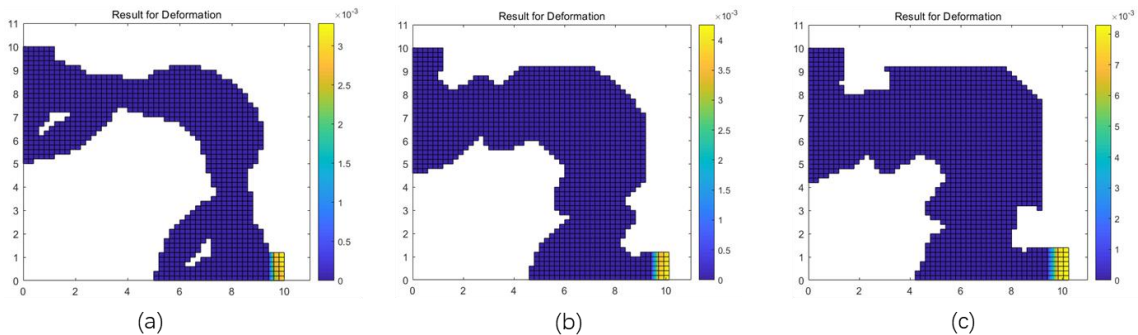


Figure 3: Microscopic heat deformation diagram of composite joints for (a) microstructure1 ;(b) microstructure2; (c) microstructure3.

3 HYBRID LATTICE STRUCTURE DESIGN BASED ON ORDERED SIMP

This section describes the topology optimization on a macroscale; the optimization model can be expressed as:

$$\begin{cases} \min: c(\boldsymbol{\rho}) = \mathbf{u}^T \mathbf{K} \mathbf{u} = \sum_{e=1}^{NE} \mathbf{u}_e^T \mathbf{k}_e(\rho_e) \mathbf{u}_e \\ \mathbf{K} \mathbf{U} = \mathbf{F} \\ \text{subject to: } \begin{cases} V(\boldsymbol{\rho}) = \frac{1}{V_0} \sum_{e=1}^N \rho_e v_e \leq VF_{set} \\ \rho_{min} \leq \rho \leq 1 \end{cases} \end{cases} \quad (3.1)$$

where c is the structural compliance; \mathbf{K} , \mathbf{U} , and \mathbf{F} are the global stiffness matrix, displacement vector, and force vector, respectively; \mathbf{k}_e is the elementary stiffness matrix, which can be expressed by:

$$\mathbf{k}_e = \mathbf{B}^T \mathbf{C}_e \mathbf{B} \tag{3.2}$$

\mathbf{B} denotes the strain-displacement matrix and \mathbf{C}_e is the homogenized elastic tensor obtained from the previous section. V_0 is the volume of the whole domain, $V_{F_{set}}$ presents the predefined volume fraction.

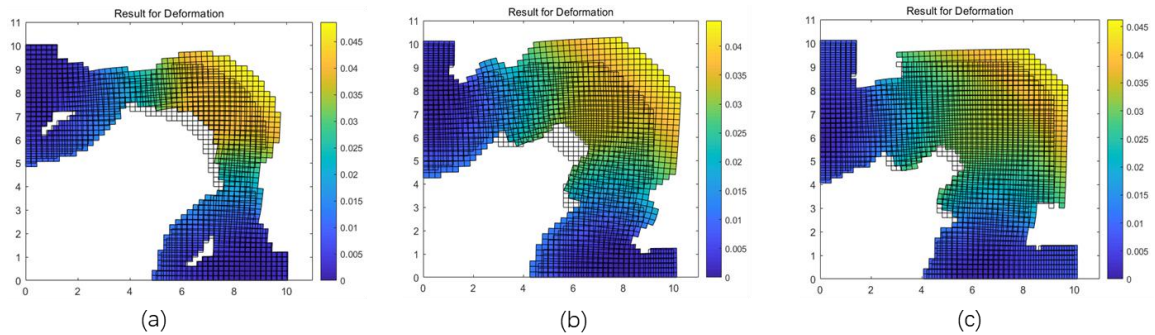


Figure 4: Microstructure overall heat deformation diagram for (a) microstructure1 ;(b) microstructure2; (c) microstructure3.

In this work, the designed functional microstructures can be treated as anisotropic materials. Therefore, all the elastic tensor terms could be interpolated by ordered SIMP.

In ordered SIMP, multi-microstructures are sorted in the ascending order of their corresponding material density ρ_i^T (as depicted in Figure 5). Then, the material densities are normalized as:

$$\rho_i = \frac{\rho_i^T}{\rho_{max}} \tag{3.3}$$

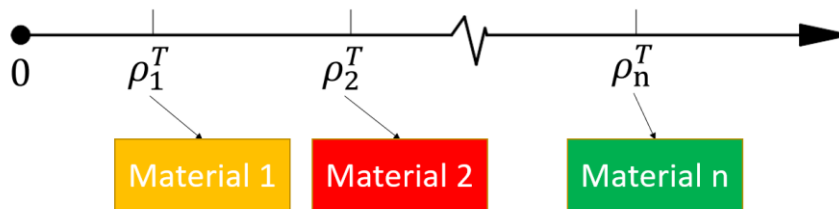


Figure 5: Illustration of the density-based material sorting.

ρ_{max} is the density for the stiffest microstructure; it should be noted that the density of two solid materials that compose the microstructure is assumed to be the same, so the density of the corresponding microstructure is determined by the sum volume fraction of two solid materials. The three microstructures with three normalized densities $\rho_i = [0, \frac{2}{3}, \frac{5}{6}, 1]$ shown in Table 2. are all used in this work, then the elastic tensor is presented below,

$$\mathbf{C}_e = \boldsymbol{\eta}(\rho_e) \cdot \mathbf{C}_{max}^H = \begin{bmatrix} \eta_{11}(\rho_e) \cdot C_{11}^H & \eta_{12}(\rho_e) \cdot C_{12}^H & 0 \\ \eta_{21}(\rho_e) \cdot C_{21}^H & \eta_{22}(\rho_e) \cdot C_{22}^H & 0 \\ 0 & 0 & \eta_{33}(\rho_e) \cdot C_{33}^H \end{bmatrix} \tag{3.4}$$

where \mathbf{C}_{max}^H is the effective elastic tensor for the stiffest microstructure, $\boldsymbol{\eta}(\rho_e)$ is the ordered SIMP interpolation function, which is given as

$$\boldsymbol{\eta}(\rho_e) = \left(\frac{\rho_e - \rho_i}{\rho_{i+1} - \rho_i} \right)^P \cdot \left(\frac{\mathbf{C}_{i+1}^H - \mathbf{C}_i^H}{\mathbf{C}_{\max}^H} \right) + \frac{\mathbf{C}_i^H}{\mathbf{C}_{\max}^H}, \rho_e \in [\rho_i, \rho_{i+1}] \tag{3.5}$$

where \mathbf{C}_i^H indicates the effective elastic tensor of the i^{th} microstructure; P is the penalty coefficient. In this work, P is set to be 3.

The interpolation curves of the normalized elastic modulus with respect to the density variable are shown in Figure 6.

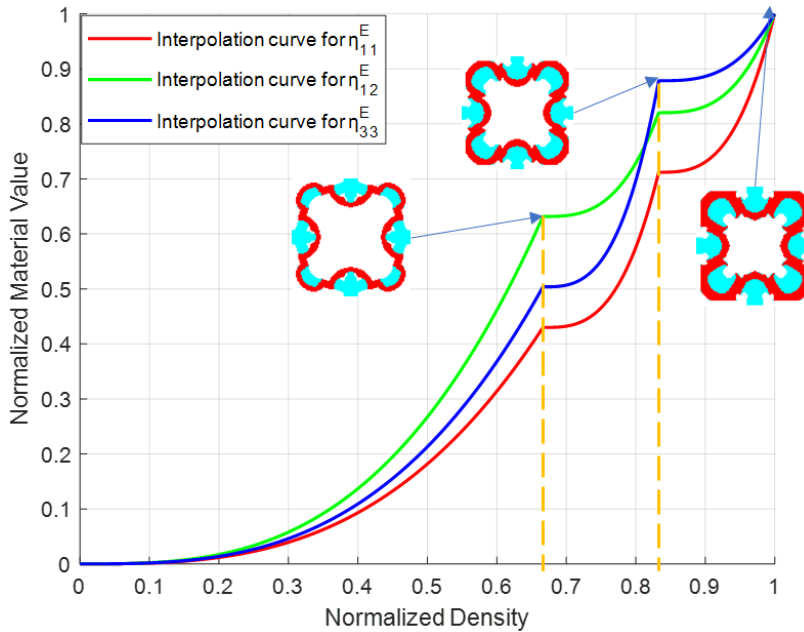


Figure 6: The interpolation curves for η^E .

4 SENSITIVITY ANALYSIS

This topology optimization is solved based on sensitivities using the method of moving asymptotes (MMA), which requires first-order sensitivity information of the constraints and the objective function. In the following, a critical derivative of the sensitivity analysis is presented.

4.1 Sensitivity Analysis for Microscale

Considering that the design variable x is independent of the design variables, and the two design variables are equivalent, the derivation processes are the similar for both design variables. Therefore, it only needs to present the sensitivity of the design variable x here. The objective function $\frac{\partial f}{\partial x}$ can be presented below:

$$\frac{\partial f}{\partial x} = 2 \frac{\partial \alpha_{11}^H(x,y)}{\partial x} + 2 \frac{\partial \alpha_{22}^H(x,y)}{\partial x} \tag{4.1}$$

where $\frac{\partial \alpha_{pq}^H}{\partial x}$ can be derived from Eq. (2.9)

$$\frac{\partial \alpha_{pq}^H}{\partial x} = \mathbf{C}_{pqrs}^H^{-1} \left(\frac{\partial \beta_{rs}^H}{\partial x} - \frac{\partial \mathbf{C}_{pqrs}^H}{\partial x} \alpha_{pq}^H \right) \tag{4.2}$$

Applying chain rule and Eq. (2.4)

$$\frac{\partial \mathbf{B}_{pq}^H}{\partial \mathbf{x}} = \frac{1}{|V|} \int \frac{\partial \mathbf{C}_{pqrs}^e}{\partial \mathbf{x}} (\alpha_{pq}^e - \varepsilon_{pq}) (\varepsilon_{rs}^{0(ij)} - \varepsilon_{rs}^{(ij)}) dV + \frac{1}{|V|} \int \mathbf{C}_{pqrs}^e \frac{\partial \alpha_{pq}^e}{\partial \mathbf{x}} (\varepsilon_{rs}^{0(ij)} - \varepsilon_{rs}^{(ij)}) dV \quad (4.3)$$

And $\frac{\partial \mathbf{C}_{pqrs}^H}{\partial \mathbf{x}}$ can be derived from Eq. (2.3)

$$\frac{\partial \mathbf{C}_{pqrs}^H}{\partial \mathbf{x}} = \frac{1}{|V|} \int \frac{\partial \mathbf{C}_{pqrs}^e}{\partial \mathbf{x}} (\varepsilon_{pq}^{0(ij)} - \varepsilon_{pq}^{(ij)}) (\varepsilon_{rs}^{0(ij)} - \varepsilon_{rs}^{(ij)}) dV \quad (4.4)$$

As for $\frac{\partial \mathbf{C}_{pqrs}^e}{\partial \mathbf{x}}$ and $\frac{\partial \alpha_{pq}^e}{\partial \mathbf{x}}$, it can be given from Eq. (2.7) and Eq. (2.8) respectively. And it is different for derivation of design variables x and y here.

$$\frac{\partial \mathbf{C}_{pqrs}^e}{\partial x} = P x_e^{P-1} \cdot (y_e^P \cdot \mathbf{C}_{pqrs}^2 + (1 - y_e)^P \cdot \mathbf{C}_{pqrs}^1) \quad (4.5)$$

$$\frac{\partial \mathbf{C}_{pqrs}^e}{\partial y} = x_e^P \cdot (P y_e^{P-1} \cdot \mathbf{C}_{pqrs}^2 - P(1 - y_e)^{P-1} \cdot \mathbf{C}_{pqrs}^1) \quad (4.6)$$

$$\frac{\partial \alpha_{pq}^e}{\partial x} = 0 \quad (4.7)$$

$$\frac{\partial \alpha_{pq}^e}{\partial y} = P y_e^{P-1} \cdot \alpha_{ij}^2 - P(1 - y_e)^{P-1} \cdot \alpha_{ij}^1 \quad (4.8)$$

up until now, the sensitivity of objective function can be obtained by using the chain rule with the above derivations. Three constraints sensitivities are presented below.

$$\frac{\partial V_1}{\partial \mathbf{x}} = \frac{1}{V} \sum_{e=1}^{NE} (1 - y_e) v_e \quad (4.9)$$

$$\frac{\partial V_2}{\partial \mathbf{x}} = \frac{1}{V} \sum_{e=1}^{NE} y_e v_e \quad (4.10)$$

$$\frac{\partial K}{\partial \mathbf{x}} = 0.25 \left(\frac{\partial \alpha_{11}^H}{\partial \mathbf{x}} + \frac{\partial \alpha_{12}^H}{\partial \mathbf{x}} + \frac{\partial \alpha_{21}^H}{\partial \mathbf{x}} + \frac{\partial \alpha_{22}^H}{\partial \mathbf{x}} \right) \quad (4.11)$$

4.2 Sensitivity Analysis for Macroscale

At the macroscale, the objective function is structural compliance. Combining Eq. (3.2) and Eq. (3.4). $\frac{\partial c}{\partial \rho_e}$ can be presented below:

$$\frac{\partial c}{\partial \rho_e} = \frac{\partial \sum_{e=1}^N \mathbf{u}_e^T \mathbf{B}_e^T \eta(\rho_e) \cdot \mathbf{C}_{\max}^H \mathbf{B}_e \mathbf{u}_e}{\partial \rho_e} = \sum_{e=1}^{NE} \mathbf{u}_e^T \mathbf{B}_e^T \frac{\partial \eta(\rho_e)}{\partial \rho_e} \cdot \mathbf{C}_{\max}^H \mathbf{B}_e \mathbf{u}_e \quad (4.12)$$

Then the $\frac{\partial \eta(\rho_e)}{\partial \rho_e}$ can be derived from Eq. (3.5).

$$\frac{\partial \eta(\rho_e)}{\partial \rho_e} = P \left(\frac{\rho_e - \rho_i}{\rho_{i+1} - \rho_i} \right)^{P-1} \left(\frac{\mathbf{C}_{i+1}^H - \mathbf{C}_i^H}{\mathbf{C}_{\max}^H} \right) \quad (4.13)$$

For the sensitivity of the volume constraint.

$$\frac{\partial V}{\partial \rho_e} = \sum_{e=1}^{NE} v_e \quad (4.14)$$

In addition, in topology optimization, filters are usually used to eliminate checkboard and projections to make the result converge to 0 or 1, eliminating intermediate values. This paper uses PDE filter and Heaviside projection, but this is not the innovation and focus of this paper, interested readers can refer to [8, 18].

5 CASE STUDY

5.1 L-bracket Benchmark

This section validates the proposed method with a classical 2-D L-bracket benchmark, as shown in Figure 7. In this example, 50×50 4-node quadrilateral elements are adopted. The top edge of the L-bracket is clamped, and a vertical load $F=4500\text{N}$ is exerted to the right-side upper corner. Note that the load is distributed over six nodes to avoid stress concentration. In these cases, the initial value of design variables is set to be 0.5, and the filter radius is 2 element sizes. The iterative process will terminate when no further improvement of the objective function can be achieved. Namely, the difference of the objective values between two adjacent iterations is less than 0.01 in 20 steps, or the maximum iteration number (250) is exceeded.

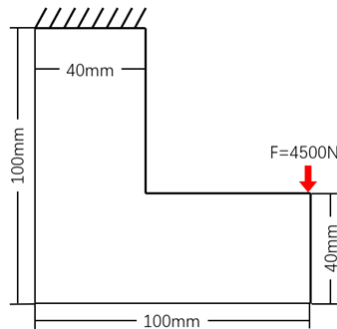


Figure 7: The boundary conditions for the L-Bracket.

Figure 8(a) presents the microstructure distribution and optimal structure. The structure thermal distortion under a temperature difference of 30°C is shown in Figure 8(b). The maximum displacement is 0.01856 mm , and the compliance of the whole structure is $c = 2.5725$. To make a comparison, Figure 8(c) shows the optimal result only with solid material 1 under the same volume fraction ($VF_{\text{Set}} = 0.5$), and the compliance is $c = 3.1572$. The maximum thermal distortion is 0.2427 mm , as indicated in Figure 8(d). The experiment results validate that the proposed method could design structures with higher stiffness and substantially reduced structural thermal distortion compared to the structure optimized with the conventional approach.

Figure 9 presents the full-scale structure of optimal results with multi-microstructures. Figure 10 demonstrates the converge history of the optimization process; it shows the compliance finally converges at 2.5725, while the maximum heat displacement finally converges at 0.01856 mm .

5.2 MBB-beam

This section applied this approach in the design of the MBB-beam. The size and boundary conditions of the MBB-beam are shown in Figure 11. Its length is 480mm, and the width is 100mm. A 100N load is applied at the center of the top edge. The left and right bottom corners are fixed. Since MBB-beam is symmetric, so only half of the MBB-beam is needed to be analyzed to save the computational cost. The design domain is meshed with 50×120 four-node quadrilateral elements. The initial set and the convergence conditions are the same as that in section 5.1.

Figure 12(a) gives the microstructure distribution and optimal macrostructure. The structure thermal distortion under a temperature difference of 30°C is shown in Figure 12(b).

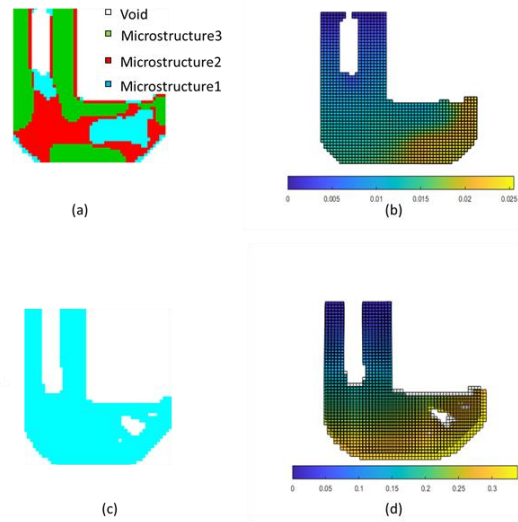


Figure 8: (a)The optimal result with multi-microstructures and (b) its thermal expansion ($\Delta T=30^{\circ}C$); (c) The optimal result only with solid material 1 and (d) its thermal expansion ($\Delta T=30^{\circ}C$) (L-Bracket).

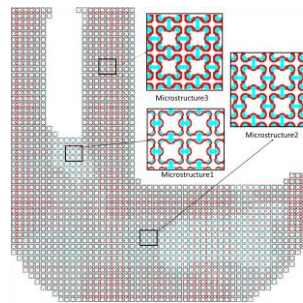


Figure 9: The final full-scale design result (L-Bracket).

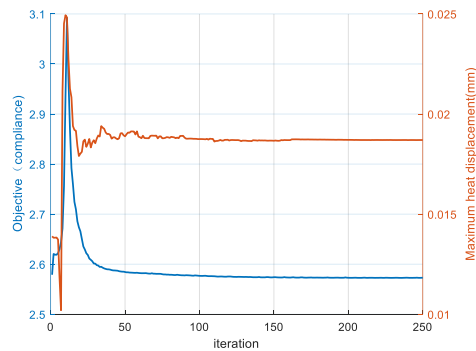


Figure 10: The convergence history for the objective value (left), and the convergence history for the maximum heat displacement (right) (L-Bracket).

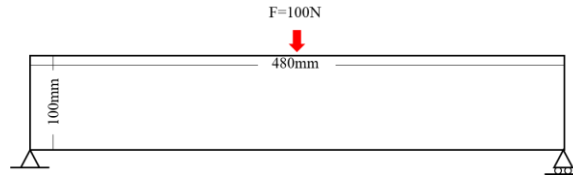


Figure 11: The boundary conditions for MBB-beam.

The maximum displacement is 0.03258 mm , and the compliance of the whole structure is $c = 0.6913$. Similar to section 5.1, Figure 12(c). shows the optimal result only with solid material 1 under the same volume fraction ($VF_{\text{Set}} = 0.5$), and the compliance is $c = 0.7115$. The maximum thermal distortion is 0.3581mm .

Figure 13 presents the full-scale structure of optimal results with multi-microstructures. Figure 14 is the converged history of the optimization process.

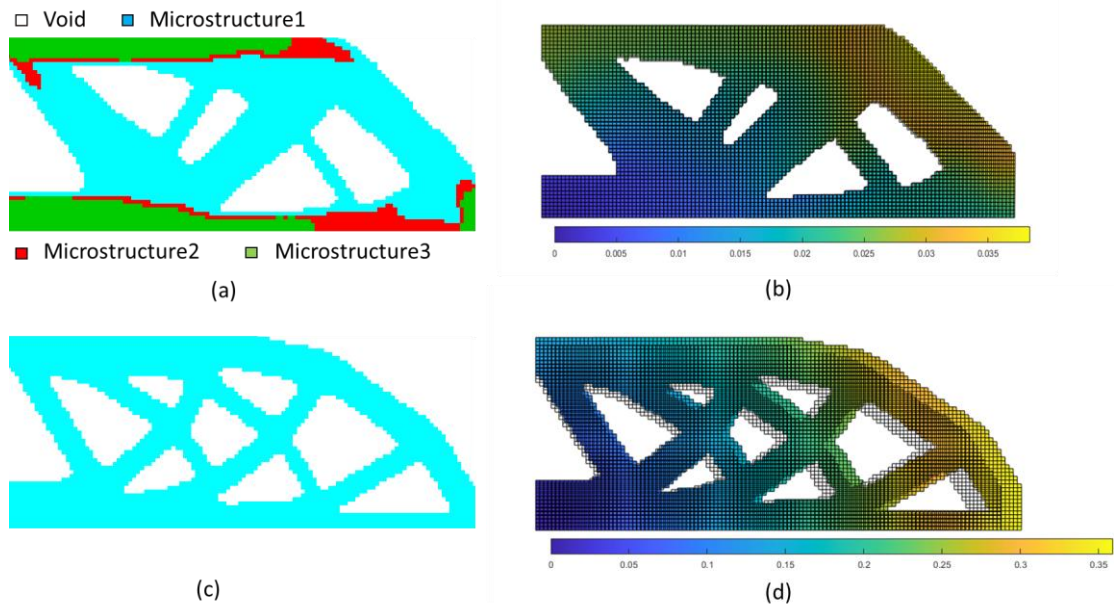


Figure 12: (a) The optimal result with multi-microstructures and (b) its thermal expansion ($\Delta T = 30^\circ\text{C}$); (c) The optimal result only with solid material 1 and (d) its thermal expansion ($\Delta T = 30^\circ\text{C}$) (MBB-beam).

5.3 Computational Time

The computational time is briefly discussed in this section. All the above cases were run on a desktop computer with AMD Core R9 5900X CPU and 32GB RAM. For microstructures design, it takes 10.15s per iteration. The homogenization method takes 87.1% time, and the MMA solver accounts for 6.8%. The rest time is for results plot. As to macrostructure design, taking the case in section 5.1 as an example, the average time spent per iteration was 7.35s: the FEM part accounted for 46.3%, the sensitivity analysis part takes 23.4%, and the MMA solver takes 18.2%, and the rest accounted for the results plot. For another cases, the percentage of each part is similar, but for more elements, such as 50×120 in section 5.2, the time spent per iteration is up to 11.32s.

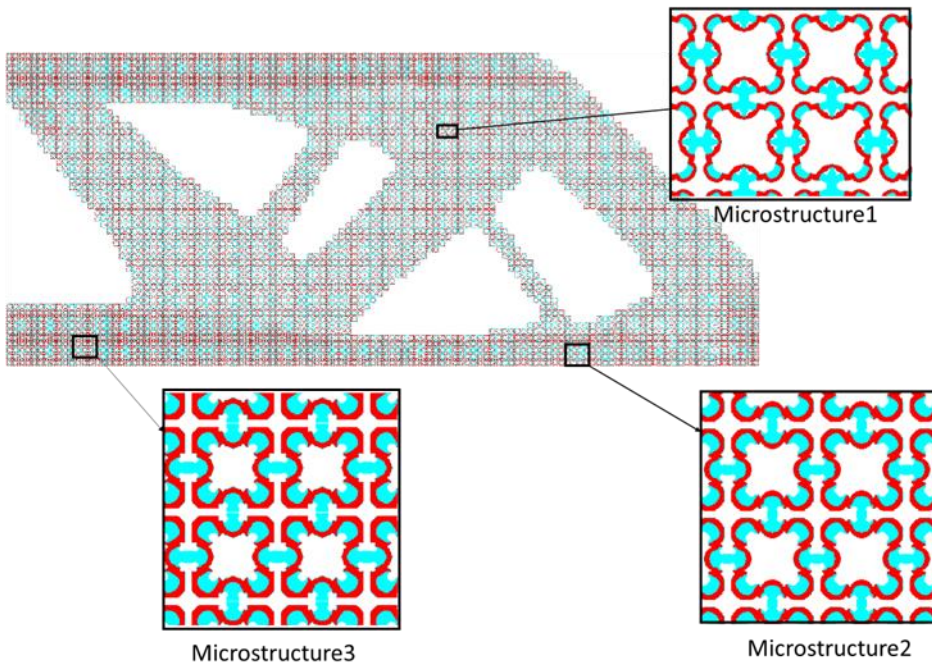


Figure 13: The final full-scale design result (MBB-beam).

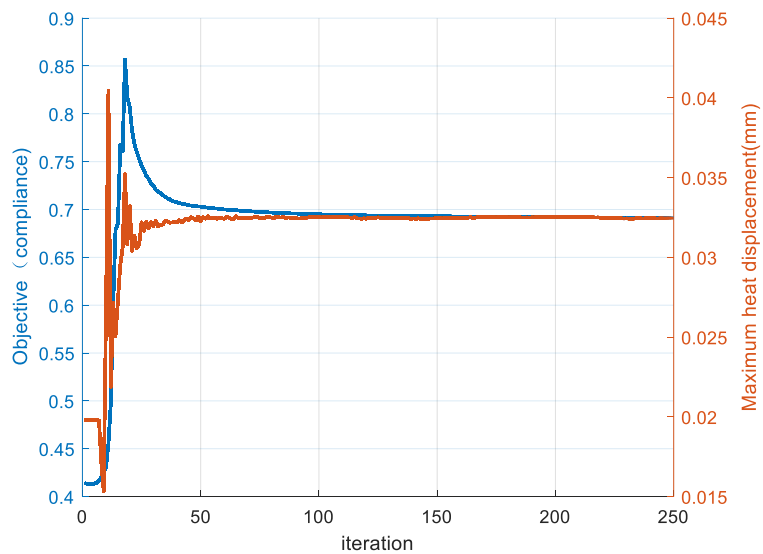


Figure 14: The convergence history for the objective value (left), and the convergence history for the maximum heat displacement (right) (MBB-beam).

6 CONCLUSION:

This work proposed a method based on topological optimization and homogenization theory to design hybrid lattice structures with multiple functional microstructure configurations. To verify the effectiveness of this approach, microstructures with zero thermal expansion were obtained in this work, and it is used to design the optimal stiffness hybrid lattice structure. The final case study shows the structure obtained by this method did have the advantage of being more stiffness and less thermally expanded than the results obtained from the optimization of pure materials.

There is still additional space to extend the current work. For the obtained structure, it could be further optimized, such as using the possibly genetic algorithm to further optimize the resulting structures and remove unnecessary materia [17]. In addition to the simulation verification, experimental verification is often more convincing. However, the authors' existing experimental equipment and conditions are insufficient to support this experiment. Besides, this paper considers only the two-dimensional case due to the limited computational power. And the three-dimensional structure is more realistic. Therefore, it will be purposefully extended to the three-dimensional case in our future work. Finally, machinability is an indispensable consideration in putting this method into practice. For the structure designed so far, the manufacturing difficulty is vast. The algorithm should sacrifice some of its performance to improve its machinability in the next work, then have a comparison to real manufactured structures.

ACKNOWLEDGEMENTS

This work was supported by the China Scholarship Council under Grant CSC 202008440546 and the NSERC funding (NSERC RGPIN-2017-04516 Ahmad).

Yifan Guo, <http://orcid.org/0000-0002-3078-9968>

Yongsheng Ma, <http://orcid.org/0000-0002-6155-0167>

Rafiq Ahmad, <http://orcid.org/0000-0001-9353-3380>

REFERENCES

- [1] Ajdari, A.; Nayeb-Hashemi, H.; Vaziri, A.: Dynamic crushing and energy absorption of regular, irregular and functionally graded cellular structures, *International Journal of Solids and Structures*, 48, 2011, 506-516. <https://doi.org/10.1016/j.ijsolstr.2010.10.018>
- [2] Andreassen, E.; Andreassen, C. S.: How to determine composite material properties using numerical homogenization, *Computational Materials Science*, 83, 2014, 488-495. <https://doi.org/10.1016/j.commatsci.2013.09.006>
- [3] Cheng, L.; Zhang, P.; Biyikli, E.; Bai, J.; Robbins, J.; To, A.: Efficient design optimization of variable-density cellular structures for additive manufacturing: theory and experimental validation, *Rapid Prototyping Journal*, 2017, <https://doi.org/10.1108/RPJ-04-2016-0069>
- [4] Dove, M. T.; Fang, H.: Negative thermal expansion and associated anomalous physical properties: review of the lattice dynamics theoretical foundation, *Reports on Progress in Physics*, 79, 2016, 066503. <https://doi.org/10.1088/0034-4885/79/6/066503>
- [5] Elnasri, I.; Pattofatto, S.; Zhao, H.; Tsitsiris, H.; Hild, F.; Girard, Y.: Shock enhancement of cellular structures under impact loading: Part I Experiments, *Journal of the Mechanics and Physics of Solids*, 55, 2007, 2652-2671. <https://doi.org/10.1016/j.jmps.2007.04.005>
- [6] Helou, M.; Kara, S.: Design, analysis and manufacturing of lattice structures: an overview, *International Journal of Computer Integrated Manufacturing*, 31, 2018, 243-261. <https://doi.org/10.1080/0951192X.2017.1407456>
- [7] Kovachki, N.; Liu, B.; Sun, X.; Zhou, H.; Bhattacharya, K.; Ortiz, M.; Stuart, A.: Multiscale modeling of materials: Computing, data science, uncertainty and goal-oriented optimization, *Mechanics of Materials*, 165, 2022, 104156. <https://doi.org/10.1016/j.mechmat.2021.104156>

- [8] Lazarov, B. S.; Sigmund, O.: Filters in topology optimization based on Helmholtz - type differential equations, *International Journal for Numerical Methods in Engineering*, 86, 2011, 765-781. <https://doi.org/10.1002/nme.3072>
- [9] Markl, M.; Körner, C.: Multiscale modeling of powder bed-based additive manufacturing, *Annual Review of Materials Research*, 46, 2016, 93-123. <https://doi.org/10.1146/annurev-matsci-070115-032158>
- [10] Moreira, J. B. D.; de Souza Lisboa, E.; Rodrigues, G. C.; Link, F. B.; Casas, W. J. P.: Multiscale topology optimization for frequency domain response with bi-material interpolation schemes, *Optimization and Engineering*, 22, 2021, 2707-2739. <https://doi.org/10.1007/s11081-020-09550-7>
- [11] Saxena, K. K.; Das, R.; Calius, E. P.: Three decades of auxetics research— materials with negative Poisson's ratio: a review, *Advanced Engineering Materials*, 18, 2016, 1847-1870. <https://doi.org/10.1002/adem.201600053>
- [12] Sigmund, O.; Torquato, S.: Design of materials with extreme thermal expansion using a three-phase topology optimization method, *Journal of the Mechanics and Physics of Solids*, 45, 1997, 1037-1067. <https://doi.org/10.1007/s00158-013-0978-6>
- [13] Sigmund, O.; Maute, K.: Topology optimization approaches, *Structural and Multidisciplinary Optimization*, 48, 2013, 1031-1055. [https://doi.org/10.1016/S0022-5096\(96\)00114-7](https://doi.org/10.1016/S0022-5096(96)00114-7)
- [14] Svanberg, K.: The method of moving asymptotes—a new method for structural optimization, *International journal for numerical methods in engineering*, 24, 1987, 359-373.
- [15] Tao, W.; Leu, M. C.: Design of lattice structure for additive manufacturing, *Journal*, 2016, 325-332. <https://doi.org/10.1109/ISFA.2016.7790182>
- [16] Vaissier, B.; Pernot, J.-P.; Chougrani, L.; Véron, P.: Parametric design of graded truss lattice structures for enhanced thermal dissipation, *Computer-Aided Design*, 115, 2019, 1-12. <https://doi.org/10.1016/j.cad.2019.05.022>
- [17] Vaissier, B.; Pernot, J.-P.; Chougrani, L.; Véron, P.: Genetic-algorithm based framework for lattice support structure optimization in additive manufacturing, *Computer-Aided Design*, 110, 2019, 11-23. <https://doi.org/10.1016/j.cad.2018.12.007>
- [18] Wang, F.; Lazarov, B. S.; Sigmund, O.: On projection methods, convergence and robust formulations in topology optimization, *Structural and Multidisciplinary Optimization*, 43, 2011, 767-784. <https://doi.org/10.1007/s00158-010-0602-y>
- [19] Wu, J.; Sigmund, O.; Groen, J. P.: Topology optimization of multi-scale structures: a review, *Structural and Multidisciplinary Optimization*, 63, 2021, 1455-1480. <https://doi.org/10.1007/s00158-021-02881-8>
- [20] Xia, L.; Breitkopf, P.: Design of materials using topology optimization and energy-based homogenization approach in Matlab, *Structural and multidisciplinary optimization*, 52, 2015, 1229-1241. <https://doi.org/10.1007/s00158-015-1294-0>
- [21] Xia, L.; Breitkopf, P.: Recent advances on topology optimization of multiscale nonlinear structures, *Archives of Computational Methods in Engineering*, 24, 2017, 227-249. <https://doi.org/10.1007/s11831-016-9170-7>
- [22] Xie, Y. M.; Yang, X.; Shen, J.; Yan, X.; Ghaedizadeh, A.; Rong, J.; Huang, X.; Zhou, S.: Designing orthotropic materials for negative or zero compressibility, *International Journal of Solids and Structures*, 51, 2014, 4038-4051. <https://doi.org/10.1016/j.ijsolstr.2014.07.024>
- [23] Xu, S.; Liu, J.; Zou, B.; Li, Q.; Ma, Y.: Stress constrained multi-material topology optimization with the ordered SIMP method, *Computer Methods in Applied Mechanics and Engineering*, 373, 2021, 113453. <https://doi.org/10.1016/j.cma.2020.113453>
- [24] Zuo, W.; Saitou, K.: Multi-material topology optimization using ordered SIMP interpolation, *Structural and Multidisciplinary Optimization*, 55, 2017, 477-491. <https://doi.org/10.1007/s00158-016-1513-3>